PAPER

Check for updates

Preparation of ZIF-8-based nanocomposites and their notable antibacterial activities†

Le Hong Tho, [ID] [ab] Do Thao Anh, [ab] Hanh Kieu Thi Ta, [abc] Bang Thang Phan, [ID] [ab] Sungkyun Park, [d] Seyoung Kwon, [d] Kieu The Loan Trinh [ID] [ab] and Nhu Hoa Thi Tran [ID] *[bc]

Recent deaths related to antimicrobial resistance have raised alarms for global human health. To overcome this issue, extensive research concentrating on developing novel antibacterial strategies, materials, and methods is needed. In this work, we provide a breakthrough combination of ZIF-8 with silver nanoparticles (Ag NPs), gold NPs (Au NPs), or magnetic iron oxide NPs (Fe$_3$O$_4$ NPs). The obtained nanocomposites were evaluated for essential properties *via* XRD, UV-vis spectroscopy, FESEM, EDS, VSM, and HRTEM techniques. They also demonstrated remarkable antibacterial activities toward two typical pathogenic bacteria, *Escherichia coli* and *Staphylococcus aureus*. Interestingly, the investigated materials' liquid and solid states exhibited superior inhibition zones, with the maximum observed value of 30.7 mm. Thus, our synthesized nanomaterials may show great potential for the application of further strategies in the biomedical field.

1. Introduction

The widespread use of antibiotics has extensively accelerated drug resistance-related mortality, raising alarms for public health worldwide. Recently, antimicrobial resistance (AMR) has been globally considered as one of the top ten health threats to humans.[1] In 2019 and 2021, 9 million people were estimated to die from bacterial infections, with approximately 5 million cases related to AMR each year.[2] The number of cases is expected to increase by over 10 million by 2050, according to the World Health Organization (WHO). Among the bacterial pathogens that show resistance to various available as well as at-risk broad-spectrum antibiotics, *Escherichia coli* and *Staphylococcus aureus* are the most concerning ones.[3] The regions predicted to attain the highest related AMR mortality rates in any age group up to 2050 are Latin America, South Asia, and the Caribbean.[2] Moreover, the gross domestic product would globally reduce by approximately 4% by 2050, as reported by the World Bank.[1] Therefore, AMR has been proposed as one of the most considerable challenges of the 21st century.[2] Numerous

endeavors in proposing and conducting experimental trials have attracted researchers to determine strategies to deal with AMR.

Developing novel nanomaterials with notable antimicrobial properties has stood out as one of the best alternative for bacterial treatment. Metal–organic frameworks (MOFs) have lately received considerable attention owing to their ultra-high surface area, superior porosity, and interesting antimicrobial activities, revealing their developmental potential in infection diagnoses or treatments.[4–6] There have been more than 20 000 reported and synthesized MOFs since the discovery of the first MOF in the 1990s.[7] Interestingly, with the diversity of the amounts of intrinsic metal ions and organic ligands, flexibility in surface modification, tunability in morphology, pore size, biocompatibility, and biodegradability, MOFs as well as their derivatives' composites with other types of nanomaterials can be used for various antibacterial applications, including food preservation, wound healing, drug delivery, bioimaging, diagnosis, wastewater treatment, and recycling.[8–12]

The remarkable thermal and chemical stabilities of zeolitic imidazolate frameworks (ZIFs),[13] a representative subclass of MOFs, together with enhancement in the antibacterial activities of conventional metal nanoparticles and metal oxide nanoparticles, have fascinated researchers. ZIF-8 nanostructures are composed of divalent zinc ions (Zn^{2+}) and heterocyclic imidazolyl organic ligands, which are reported to act as antibiotics or assist in gradual ionic leaching, an important antimicrobial process during growth inhibition and eventually bacterial killing.[14] Moreover, varied scholars demonstrated that ZIF-8 and its combination with other nanoparticles, particularly

[a] Center for Innovative Materials and Architectures, Ho Chi Minh City 700000, Vietnam

[b] Vietnam National University, Ho Chi Minh City 700000, Vietnam

[c] Faculty of Materials Science and Technology, University of Science, Ho Chi Minh City 700000, Vietnam. E-mail: ttnhoa@hcmus.edu.vn

[d] Department of Physics, Pusan National University, Busan 46241, Republic of Korea

† Electronic supplementary information (ESI) available. See DOI: https://doi.org/10.1039/d5ma00177c

Ag, Au, and Fe_3O_4 NPs, exhibited outstanding antibacterial properties due to small size, dense surface electron density, mimicking catalysis, severe reactive oxygen species (ROS) generation leading to conformational changes of enzymes, functional inhibitions of protein, DNA, RNA, membrane damages, etc.[14–18] Hence, there should be a comparative study on ZIF-8-based nanocomposites to light up multiple proper choices for bacterial treatments.

In this work, we propose several procedures for synthesizing ZIF-8 nanostructures incorporated with Ag NPs, Au NPs, and Fe_3O_4 NPs, which are, respectively, designated as AgZ, AuZ, and MZ. Commonly, ZIF-8-based composites are fabricated by well dispersing ZIF-8 powder in a solution of precursors for nanoparticle synthesis and allowing wet chemical reaction to occur.[19] However, this strategy seems inappropriate for bioapplications because of the hazardous potential risks of excess metallic ions within the ZIF-8 pores. With the aim to optimize the biosafety as well as the morphology of composites, well-defined Ag, Au, and Fe_3O_4 colloids studied by previous scholars[20–22] were used instead of metal salts or reducing agents for the prevention of ZIF-8 nanostructure collapse. By introducing those solutions in the fabrication strategies, the formation of ZIF-8 is ensured to be instantaneous with the decoration of nanoparticles thanks to the abundant organic groups on the ZIF-8 surfaces. Beyond these scopes, we specify the crucial roles of aforementioned nanoparticles in the antibacterial behaviors of the entire composite for each *via* their aggregation and incorporation state towards ZIF-8 nanostructures.

2. Experimental section

2.1 Materials

Essential reagents used in material synthesis include iron(II) chloride tetrahydrate ($FeCl_2 \cdot 4H_2O$, 99%), polyvinylpyrrolidone (PVP, Mw: 55 000, 99%), zinc nitrate hydrate ($Zn(NO_3)_2 \cdot 6H_2O$, 98%), 2-methylimidazole (Hmim, $C_6H_4N_2$, 99%), silver nitrate ($AgNO_3$, 98%), gold(III) chloride hydrate ($HAuCl_4 \cdot xH_2O$, 99%), sodium citrate tribasic dihydrate (Na_3Ctr, 99%), sodium sulfide hydrate ($Na_2S \cdot xH_2O$, >98%), ethylene glycol (EG, $C_2H_6O_2$, >99.7%), ampicillin ($C_{16}H_{19}N_3O_4S \cdot 3H_2O$), and 2,2-diphenyl-1-picrylhydrazyl (DPPH, >90%), which were supplied by Sigma Aldrich, USA. Ethanol (EtOH, C_2H_5OH, 99.8%) and methanol (MeOH, CH_3OH, 99%) were purchased from Fisher Ltd., UK. Iron(III) chloride hexahydrate ($FeCl_3 \cdot 6H_2O$, 99%) was provided by Acros Organics, USA. Sodium hydroxide (NaOH, 96%) was supplied by Guangdong Guanghua Scientific, China. All materials were of analytical grade and used without further purification.

2.2 Synthesis

Fe_3O_4 NPs, Ag NPs and Au NPs employed in this work were synthesized based on the procedures we described previously.[20–22] Basic components to construct AgZ, AuZ, and MZ nanocomposites are briefly depicted in Scheme 1.
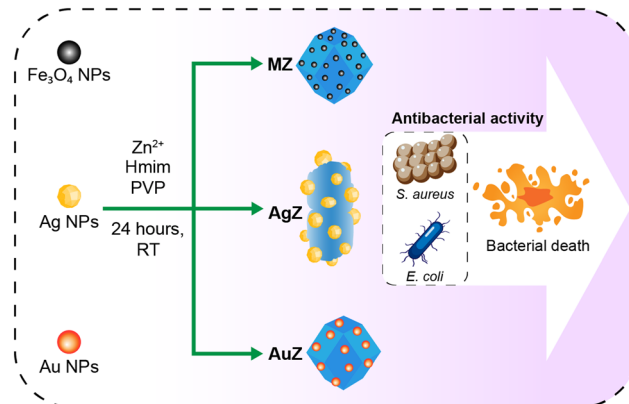
Scheme 1 Preparation of AgZ, AuZ, and MZ samples.

2.2.1 Synthesis of AgZ. A suspension of Ag NPs (8 mL, 16 mL, or 24 mL) was combined with 0.29 g of $Zn(NO_3)_2 \cdot 6H_2O$, 0.16 g of Hmim, and 0.22 g of PVP. The mixture was then stirred for 2 minutes. Following this, 32 mL of methanol was added, and the mixture was stirred continuously for 24 hours. After the reaction, the mixture was rinsed with methanol and subjected to centrifugation at 4500 rpm for 10 minutes per cycle to recover the material. The collected material was dried and dehydrated using a vacuum oven to obtain the AgZ material. The samples were labeled as AgZ (1:4), AgZ (1:2), and AgZ (3:4), respectively.

2.2.2 Synthesis of AuZ. A similar procedure to that used for synthesizing AgZ was employed to synthesize AuZ. Au NP suspensions (30 mL, 40 mL, and 60 mL) were combined with 0.356 g of $Zn(NO_3)_2 \cdot 6H_2O$, 0.197 g of Hmim, and 0.275 g of PVP, and the mixture was stirred for 2 minutes. Next, 40 mL of methanol was introduced, and the mixture was stirred continuously for 24 hours. Upon completion, the mixture was washed with methanol and centrifuged at 4500 rpm for 10 minutes per cycle to collect the material. This collected material was then dried and dehydrated in a vacuum oven to yield the AuZ composite. The resulting samples were labeled as AuZ (3:4), AuZ (1:1), and AuZ (3:2), respectively.

2.2.3 Synthesis of MZ. Briefly, a mixture of Fe_3O_4 NPs, $Zn(NO_3)_2 \cdot 6H_2O$, PVP, and Hmim was dissolved in 80 mL of methanol and stirred gently at room temperature for 24 hours. The resulting MZ nanostructures were washed with methanol *via* centrifugation and dried at 80 °C for further use. The samples were labeled MZ01, MZ03, and MZ05, corresponding to the initial amounts of Fe_3O_4 NPs used as 0.1 g, 0.3 g, and 0.5 g, respectively.

2.3 Characterization

Material characteristics were evaluated by several methods. The crystallinity was checked using a D8 Advance diffractometer (Bruker, UK) equipped with a Cu Kα X-ray source. The optical properties were determined using a V-730 UV-vis spectrophotometer (JASCO, Japan). To collect the two-dimensional (2D) figures of materials as well as elemental distribution, an S4800 field-emission scanning electron microscope (FESEM; Hitachi,

Japan) with an energy-dispersive X-ray spectrometer was used. Besides, high-resolution transmission electron microscopy (HRTEM) images were obtained using a JEM2100 (Jeol, Korea). We also used a Thermo Scientific™ K-Alpha™ X-ray photoelectron spectrometer (XPS) to obtain XPS survey and high-resolution scans of elements in fabricated materials.

2.4 Antibacterial activity assessment

The antibacterial properties of ZIF-8-based nanocomposites against *Escherichia coli* (*E. coli*, Gram-negative) and *Staphylococcus aureus* (*S. aureus*, Gram-positive) were assessed by a disk diffusion method, commonly known as the Kirby–Bauer test. The evaluation was conducted in both liquid and solid media to compare the antibacterial efficacy of the investigated materials. For solid media testing, approximately 1 mg of the material was placed on an agar plate and incubated at 37 °C for 24 hours. In liquid media, 0.5 mg of each composite was dispersed in 1 mL of deionized water, followed by sonication for 10 minutes at 30 °C. Agar plates for antimicrobial susceptibility testing were prepared by autoclaving Luria Bertani (LB) broth and agar solutions. A pure bacterial culture grown in LB broth was spread onto solidified LB agar plates. The selected materials were then applied to these plates. After inverting the plates to prevent condensation from contaminating the inoculum, they were incubated at 37 °C for 24 hours to allow bacterial growth and the formation of inhibition zones around the antimicrobial agents. The size of these inhibition zones was used to assess bacterial susceptibility in comparison with positive control using ampicillin.

In addition, we proposed the DPPH scavenging assay to evaluate the radical-scavenging (*i.e.*, antioxidant) capability of materials. First, 1 mg DPPH was diluted in 25 mL EtOH, while 5 mg synthesized materials (AgZ, AuZ, and MZ) were dispersed in 1.5 mL EtOH. Then, 100 μL nanoparticle suspensions were dropped into 2 mL DPPH solution and left undisturbed in the darkness, at room temperature for 30 minutes. Ultimately, the UV-vis spectra of mixtures were recorded, and the intensity of the characteristic peak at 517 nm was used to calculate the radical-scavenging ability (RSA) as follows:

$$\text{RSA} = \frac{A_{\text{origin}} - A_{\text{sample}}}{A_{\text{origin}}} \times 100\%, \text{ in which } A_{\text{origin}} \text{ and } A_{\text{sample}}$$

are correspondingly the absorbance at 517 nm of DPPH without and with treatments of antibacterial materials.

3. Results and discussions

3.1 Characteristics of AgZ and AuZ

As one of the most popular antimicrobial agents, Ag NPs are used to form composites with ZIF-8 and evaluated by different methods in this work. The X-ray diffraction (XRD) pattern of the AgZ material (Fig. 1a) shows some diffraction peaks of zeolite framework of ZIF-8 in the range of 0°–37° of 2θ value,[23] including 7.46°, 12.85°, 14.83°, and 18.38°. In contrast, the other diffraction angles of 9.20°, 31.82°, 34.48°, and 36.31° are slightly shifted in comparison with other studies,[24] indicating
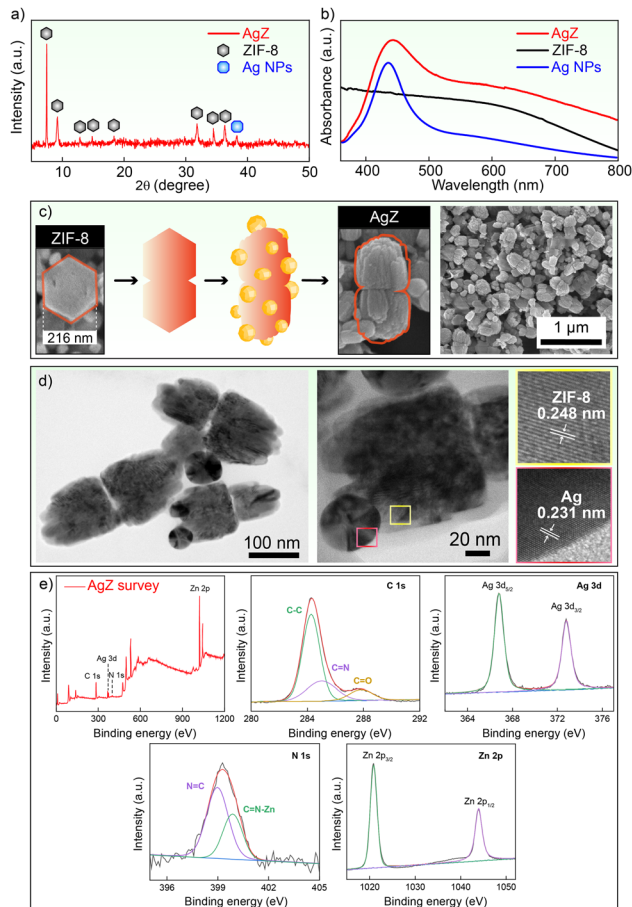

Fig. 1 Characterization of AgZ using (a) XRD, (b) UV-vis, (c) FESEM, (d) HRTEM, and (e) XPS.

the morphological change of ZIF-8 in the presence of Ag NPs. Together with the emergence of a characteristic diffraction peak of silver (111) at 38.33°, the fabricated sample is supposed to have Ag NPs in hybridized formation. Additionally, the UV-vis spectrum of AgZ suspension (Fig. 1b) indicates a strong absorption peak at 444 nm of Ag NPs, likewise a typical emerged band of ZIF-8 in the 550–700 nm region. Commonly, in the UV-vis spectrum of nanocomposites of Ag NPs and ZIF-8, or other types of MOFs generally, the SPR peak of Ag NPs seems hardly to be observed due to ZIF-8's intrinsic long-range and intense absorption.[24,25] In this work, we effectively fabricated AgZ nanocomposites with equal contributions of ZIF-8 and Ag NPs to optical absorption property, thereby providing the obvious presence of Ag NPs in AgZ.

According to some scholars, Ag⁺ cations were well dispersed in the ZIF-8 suspension and directly reduced on the surface of the ZIF-8 platform to deposit tiny Ag NPs with sizes varying from 5 nm to 30 nm.[26] This strategy has a high risk of framework collapse owing to the extreme affinity between cation Ag⁺ and linkers, which may invade the Zn²⁺-Hmim linkage and disform ZIF-8. In contrast, some research studies have used well-defined nanostructural Ag NPs and added an appropriate amount of ZIF-8's reagents to form core–shell structures.[19,27,28]

This seems more effective, in which Ag NPs with varying morphologies and sizes may combine with ZIF platforms without any disturbance in the ZIF formation. In this study, we developed AgZ nanocomposites; however, surprisingly, Ag NPs can be observed not to decorate onto ZIF-8 or assist in forming the core–shell structure. Instead, Ag NPs bind to ZIF-8 at such specific sites (Fig. 1c). The d-spacing values of ZIF-8 and Ag here are apparently observed as 0.248 nm and 0.231 nm, respectively[9] (Fig. 1d). Moreover, with the existence of Ag NPs, ZIF-8 seems to be dissimilar to the conventional rhombic dodecahedron geometry. It is because water molecules along with Ag NPs in the colloid contribute to high interfacial tension and either solvent polarity or viscosity increases, *i.e.*, providing an overwhelming barrier for the ordinary ZIF-8 crystallization.[29] Following a recently proposed mechanism of ZIF-8 formation, using cosolvent excessively affects the solvation of zinc ions and ligand deprotonation, since there is a rival in noncovalent bonding among ions and methanol or water molecules. This eventually leads to proximity-induced nucleation promoting 2D oligomerization of ZIF-8. As a result, we can observe couples of spongy flake-like ZIF-8 nanostructures bind to 80–100 nm Ag NPs at random sites, as shown in Fig. 1d. Besides, the energy-dispersive spectroscopy (EDS) mapping images (Fig. S1 and S2, ESI†) help to explicate the presence of fundamental elements such as C, N, Zn, and Ag in the composite.

For further consideration of the elemental evaluation of AgZ, the XPS spectra were also used (Fig. 1e). The XPS survey spectrum of the AgZ sample shows the presence of Zn, Ag, N, and C components. The C 1s configuration can be clarified with three distinct peaks corresponding to binding energies of 284.28 eV, 285.08 eV, and 287.88 eV, respectively. Specifically, the first peak can be attributed to C–C/C=C double bonds, the second peak to the C=N bond in the imidazole ring, and the third peak to the C=O bond from the polyvinylpyrrolidone modifier. The Ag 3d spectrum exhibits peaks at 368.10 eV and 374.10 eV, corresponding to the Ag 3d5/2 and 3d3/2 electron levels, respectively, clearly confirming the presence of metallic Ag on ZIF-8. The high-resolution XPS spectrum of N 1s shows two peaks at 398.98 eV and 399.88 eV, which attribute to the N=C and C=N–Zn bonds in the imidazole ring. Moreover, the presence of Zn^{2+} in the material is proven by the two symmetric peaks observed at 1020.88 and 1043.88 eV, corresponding to the binding energies of the Zn 2p3/2 and Zn 2p1/2 spin orbitals, respectively.

Similar to AgZ, AuZ is also considered by those mentioned characterization techniques. From Fig. 2a, intense diffraction peaks assigned to the (011), (002), (112), (013), and (222) lattice planes of ZIF-8 crystals[30] appear, but there seems to be no characteristic peak of (111) Au NPs at 38.33°. In contrast, a small absorption peak of Au NPs at 525 nm can be observed in the UV-vis spectrum of AuZ colloidal (Fig. 2b). Besides, as shown in the elemental mapping (Fig. 2c) and HRTEM (Fig. 2d) images, the existence of Au NPs is well proven. Apparently, uniform spherical 20–30 nm Au NPs are distributed on the surface of ZIF-8 with a rhombic dodecahedron shape. The corresponding 0.23 nm and 0.20 nm interplanar spacing values
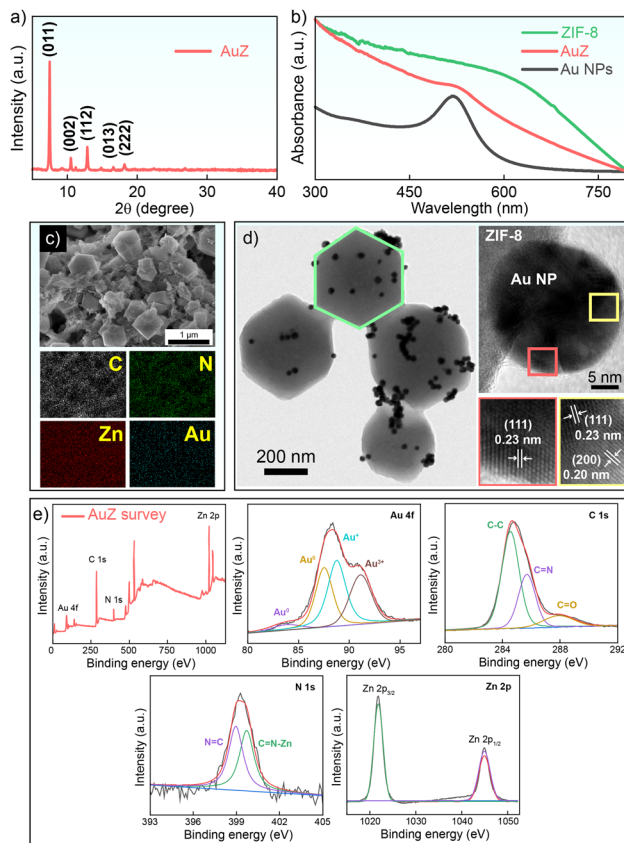

Fig. 2 Analyses of AuZ nanocomposites *via* (a) XRD, (b) UV-vis spectroscopy, (c) FESEM and EDX mapping, (d) HRTEM, and (e) XPS.

are assigned to the (111) and (200) lattice planes of Au (FCC).[31] In the composite formation, Au contributes such a small amount, *i.e.* 1.59 wt% (Fig. S3, ESI†). Due to these observed facts, the XRD pattern does not align with the UV-vis spectrum for the vital peak's appearance of tiny Au NPs.[32] Additionally, just the same as AgZ, the XPS spectra of AuZ demonstrate significant peaks corresponding to C 1s, N 1s, and Zn 2p configurations, as indicated previously. However, there are four peaks that contribute to the broadband peak in the Au 4f spectrum. This may be due to the residual Au^{3+} and Au^{1+} after centrifugation. However, the obtained AuZ nanocomposites appear to be contrary to AgZ in ZIF-8 morphology. Instead of spongy flake-like ZIF-8 as stated previously, AuZ are characterized by the conventional decoration of Au NPs on the ZIF surface. This contributes greatly to proving how pre-synthesized particles' sizes affect zeolite morphology.

3.2 Characteristics of MZ

In the process of seeking practical antibacterial materials, we found that AgZ and AuZ will not be appropriate for large-scale therapies due to noble metals' costliness and difficulties in collecting these materials after use. Instead, we chose Fe_3O_4 NPs owing to their availability, popularity, rapid preparation, and especially straightforward withdrawal by magnets. Then, we fabricated MZ samples and examined crystallinity,
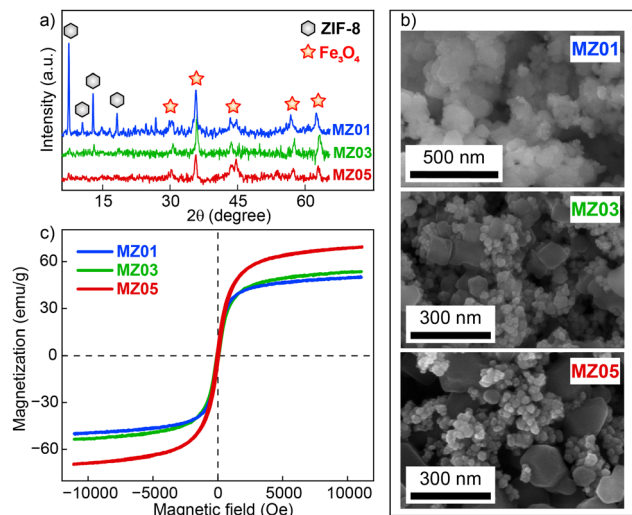
Fig. 3 FZ evaluations based on (a) XRD, (b) FESEM, and (c) VSM methods.

morphology, magnetic property, and bacterial susceptibility. Here, the key peaks of ZIF-8 and Fe_3O_4 NPs are fully shown in MZ samples' XRD patterns (Fig. 3a). Diffraction angles of (011), (002), (112), (022), (013), (222), (233), (134), and (044) lattice planes of ZIF-8 are fully demonstrated with the corresponding values of 7.52°, 10.54°, 12.92°, 14.93°, 16.61°, 18.25°, 24.61°, 26.84°, and 29.84°.[23] The other 2θ angles belong to Fe_3O_4 NPs' distinctive XRD pattern whose 30.33°, 35.77°, 43.35°, 57.21°, and 62.83° are assigned to the (220), (311), (400), (511), and (440) planes, respectively.[33] There may be no other strange XRD peaks justifying the absolute purity of MZ samples.

In Fig. 3b, the spherical Fe_3O_4 NPs incorporated with ZIF-8 have an average diameter of 30 nm, in which a change in the mass of Fe_3O_4 powder in the procedure directly affects the appearance of ZIF-8. Following our strategy, we obtained MZ nanocomposites containing a significant size of ZIF-8 in the range of 100–200 nm along with the satisfied presence of Fe_3O_4 NPs surrounding ZIF-8 without any denaturation steps. Compared to several recent scholars,[33] MZ03 and MZ05 are believed to have qualified properties on crystallinity, size, shape, and well-defined morphology of each component. Besides, as obtained from vibrating sample magnetometry (VSM) (Fig. 3c), the synthesized MZ samples can be claimed to be superparamagnetic. The coercive forces corresponding to MZ01, MZ03, and MZ05 are 37.9, 82.9, and 69.0 Oe orderly. Their magnetization saturation (M_s) values also increase from 50.4, 53.6 to 69.2 emu g^{-1}, according to the increase in Fe_3O_4 NP amounts in the composite. In comparison with our previous study,[34] MZ05 and MZ03 preserve the intrinsic M_s value of Fe_3O_4 NPs without any significant decrease despite composite formation. Thus, MZ samples, especially MZ05 and MZ03, are clarified to have satisfied magnetic properties.

3.3 Comparison of AgZ, AuZ, and MZ on antibacterial activities

The antimicrobial activity of AgZ is initially evaluated by the Kirby–Bauer disk diffusion test against *S. aureus* (Gram positive) and *E. coli* (Gram negative). A bigger diameter zone of inhibition

(ZOI) represents greater effectiveness in bacterial treatment. By investigating ZOI among samples in both solid and liquid states with different Ag NP/ZIF-8 ratios (Fig. 4a), the role of doped Ag NPs can be obviously realized through the noticed elevations in AgZ's ZOI values compared to ZIF-8. Some recent studies stated that the spongy ZIF nanostructures also help to achieve such satisfactory antimicrobial performances due to less stable morphology compared to smooth-surfaced rhombic dodecahedron or cubic shape, *i.e.* more rapid ion leaching as a result.[35,36] Besides, solid AgZ shows higher ZOI than that of the liquid one, indicating the practical capability in antibacterial surface coating, land reclamation, easy withdrawing domestic cleaning, *etc.* The highest obtained ZOI is 12.0 ± 1.7 mm belonging to solid AgZ (1:2) in the *E. coli* susceptibility test. These findings show that although with the large size of Ag NPs and ZIF-8 compared to other work,[37,38] AgZ samples demonstrate such satisfactory antibacterial activities.

Although Au NPs just contribute approximately 2 wt% to composite, the AuZ samples exhibit extraordinary ZOI values, larger than nearly 8–20 times than that of ZIF-8 (Fig. 4b). However, the increased ratio of Au NPs/ZIF-8, *i.e.* the larger amount of Au NPs, does not make ZOI higher. Considering the sensitive tendency towards *E. coli* and *S. aureus* among these ratios, liquid AuZ (3:4) showed the highest ZOI, while the solid AuZ (1:1) exhibited the best antibacterial activity. The more the Au NPs present in the composite, the greater the probability of Au NPs aggregating on the ZIF-8 surface, which seriously attenuates the antibacterial activity of materials. Throughout these observations, it is obvious that ZIF-8 plays an important role in assisting the decoration and agglomeration of Au NPs, leading to elevations in antibacterial properties. The greatest ZOI value of AuZ is 17.7 ± 0.6 mm, belonging to liquid AuZ (3:4) in *S. aureus* treatment. This bacteriostatic ring basically clarifies the excellent antimicrobial behavior, which is
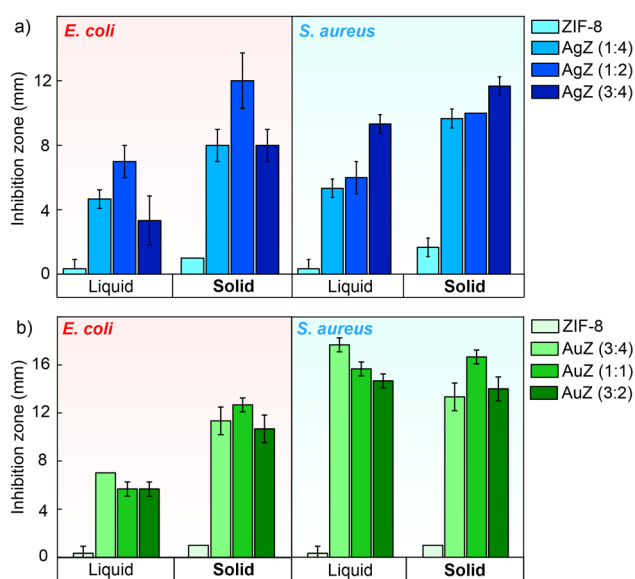

Fig. 4 Comparison of (a) AgZ and (b) AuZ samples in terms of antibacterial activities towards *E. coli* and *S. aureus*.

comparable to other recent studies.[39–41] Furthermore, AuZ acts as a better antimicrobial agent than AgZ, because of the smaller size of Au NPs, which supports their penetration through the membrane of bacteria and severe macrobiomolecule denaturations. However, Au NPs in AuZ composites are often assessed to have superior stability and biocompatibility compared to AgZ owing to the unavoidable oxidation of Ag NPs.[42] Hence, such necessary advantages of AuZ prove its huge potential in clinical trials for small-area bacterial infection treatment dealing with AMR, for instance, wound healing and bioimaging diagnosis.

As discussed previously in the VSM result, of particular interest is how effective the intrinsic magnetic property of MZ nanocomposites is. In Fig. 5a, after 30 minutes of dispersing MZ powders under aqueous conditions, they can conveniently be collected thanks to the permanent magnet. This elucidates the strong magnetic responses of MZ samples, which are favorable for clinical aqueous treatments. In comparison with ZIF-8, or even with AgZ and AuZ, MZ05 reveals such superior antibacterial activities as ZOI values are 21.7 ± 1.2 mm and 30.7 ± 1.5 mm against *E. coli* and *S. aureus*, respectively (Fig. 5b), which are higher than that of the positive control and other investigated samples (Fig. S4 and Table S1, ESI†). This can be explained by the small-sized Fe_3O_4 NPs that may easily infiltrate through the peptidoglycan cell membrane of bacteria, generate ROS, destroy organelles, and disturb the biofilm formation. Additionally, the intrinsic photo-Fenton effect of Fe_3O_4 NPs serves as the main reason for numerous hazardous radical formation within the cell.[43] The well-known accepted mechanism of the Fenton effect is written as eqn (1) and (2), in which the $^\bullet OH$ generation causes the degradation of biomacromolecules and bacterial inactivation.[44] Moreover, energy from incident photons accelerates the heterogeneous photo-Fenton process in MZ.[44] These synergistic effects contribute to the dramatic enhancement of antibacterial properties observed in MZ composites in comparison to Fe_3O_4 NPs or ZIF-8 solely. Together with ease in withdrawal after use thanks to superparamagnetic performance, our suggestion is to use antibacterial MZ samples in such large areas including wastewater or soil treatments.

$$Fe^{2+} + H_2O_2 \rightarrow Fe^{3+} + OH^- + {}^\bullet OH \quad (1)$$

$$Fe^{3+} + H_2O_2 \rightarrow Fe^{2+} + H^+ + {}^\bullet O_2H \quad (2)$$
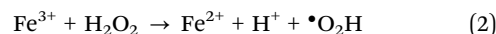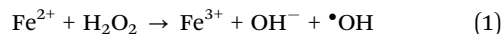
To explain more about the ROS generation of antibacterial materials, we performed the DPPH scavenging assay to indirectly assess the ROS-related behavior of the nanocomposites. Herein, the lower DPPH scavenging percentage indicates lower radical-quenching ability, and thus, stronger potential for ROS generation. As depicted in Fig. 5c, the absorbance of DPPH at 517 nm peak towards exposure to the best antibacterial performed samples of AgZ, AuZ, and MZ decreases compared to DPPH's original peak. With respect to positive control (AA), the RSA values of AgZ (3 : 4), AuZ (3 : 4), and MZ05 are 45.94%, 16.02%, and 11.14% (Fig. 5d). Apparently, MZ05 exhibited the lowest DPPH scavenging activity, *i.e.* the strongest ROS-generating capability. This correlates directly with its highest antibacterial efficacy, as previously shown by 21.7 ± 1.2 mm and 30.7 ± 1.5 mm ZOI values correspondingly against *E. coli* and *S. aureus*. These results are consistent with other scholars[45,46] on great antibacterial activities based on ROS generation of Fe_3O_4 NPs, strengthening the meaning of the combination of Fe_3O_4 NPs and ZIF-8 nanostructures.
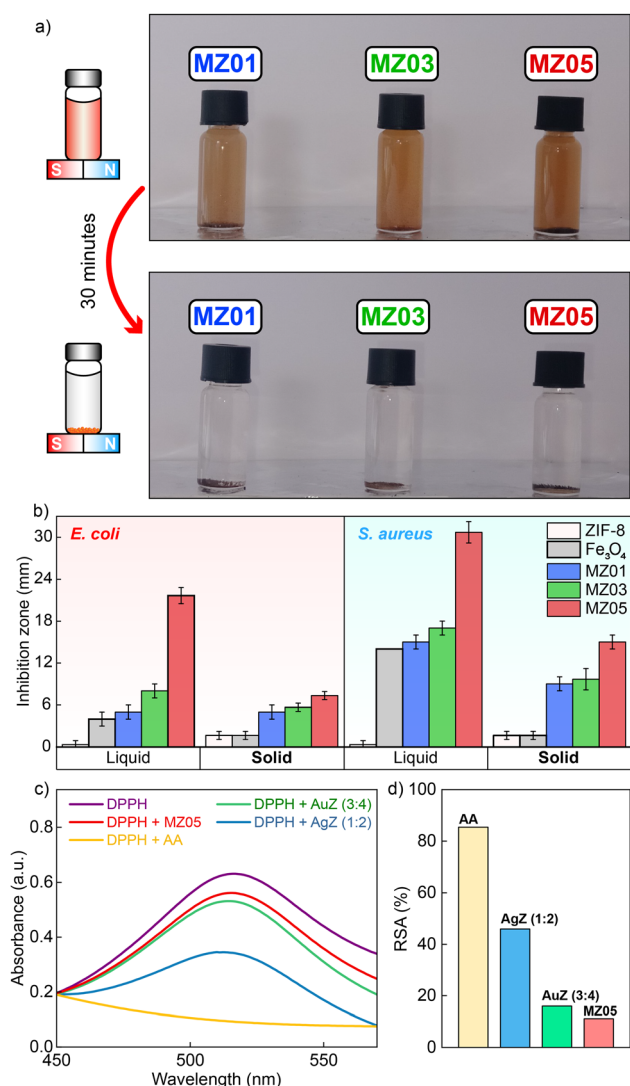

Fig. 5 (a) MZ samples' behavior in the magnetic field created by an underneath permanent magnet, (b) inhibition zones of MZ samples in comparison with ZIF-8 and Fe_3O_4 NPs, (c) UV-vis spectra of DPPH towards exposure to different substances, and (d) comparison of RSA values among samples.

4. Conclusions

In summary, our study focuses on fabricating ZIF-8-based nanocomposites showing qualified antibacterial behaviors. Throughout essential techniques, our new finding consists of AgZ nanostructures with couples of spongy flake-like ZIF-8 nanostructures binding to 80–100 nm Ag NPs. Furthermore, AuZ as well as MZ exhibit apparent combinations of rhombic dodecahedron geometric ZIF-8

and tiny spherical (roughly 30 nm) Au NPs or Fe_3O_4 NPs. AgZ, AuZ, and MZ are proven to create large inhibitions of which the greatest one is 30.7 ± 1.5 mm, observed in the *S. aureus* susceptibility test with FZ05. Both solid and liquid states of synthesized composites are mentioned to provide a more practical prospect in applying antibacterial materials. This work proposes several choices for clinical trials or suggestive directions for further studies.

Author contributions

L. H. T.: conceptualization, formal analysis, methodology, visualization, writing – reviewing and editing; D. T. A.: formal analysis, methodology, validation H. K. T. T.: data curation, formal analysis, validation B. T. P.: formal analysis, methodology, validation; S. K. P.: data curation, formal analysis; S. Y. K.: data curation, formal analysis; K. T. L. T.: data curation, formal analysis; N. H. T. T.: supervision, funding acquisition; investigation; methodology, writing – reviewing and editing.

Conflicts of interest

There are no conflicts to declare.

Data availability

The XRD and UV-vis raw data of the synthesized materials can be found below. The other supporting data were included in the ESI.†

Acknowledgements

Notes and references

1 Global Antimicrobial Resistance and Use Surveillance System (GLASS) Report 2022, World Health Organization, 2022.
2 M. Naghavi, *et al.*, *Lancet*, 2024, **404**, 1199–1226.
3 C. S. Ho, C. T. H. Wong, T. T. Aung, R. Lakshminarayanan, J. S. Mehta, S. Rauz, A. McNally, B. Kintses, S. J. Peacock, C. de la Fuente-Nunez, R. E. W. Hancock and D. S. J. Ting, *Lancet Microbe*, 2024, 100947.
4 I. W. Almanassra, L. Jaber, A. Chatla, A. Abushawish, A. Shanableh and M. Ali Atieh, *Chem. Eng. J.*, 2023, **471**, 144616.
5 K. Xu, S. Zhang, X. Zhuang, G. Zhang, Y. Tang and H. Pang, *Adv. Colloid Interface Sci.*, 2024, **323**, 103050.
6 A. Hayat, S. Rauf, B. Al Alwan, A. El Jery, N. Almuqati, S. Melhi, M. A. Amin, Y. Al-Hadeethi, M. Sohail, Y. Orooji and W. Lv, *Mater Today Energy*, 2024, **41**, 101542.
7 F. Gharagheizi, Z. Yu and D. S. Sholl, *ACS Appl. Mater. Interfaces*, 2022, **14**, 42258–42266.
8 M. Wang, X. Zhou, Y. Li, Y. Dong, J. Meng, S. Zhang, L. Xia, Z. He, L. Ren, Z. Chen and X. Zhang, *Bioact Mater*, 2022, **17**, 289–299.
9 L. Pan, T. Muhammad, L. Ma, Z. F. Huang, S. Wang, L. Wang, J. J. Zou and X. Zhang, *Appl. Catal., B*, 2016, **189**, 181–191.
10 N. T. T. Nguyen, T. T. T. Nguyen, S. Ge, R. K. Liew, D. T. C. Nguyen and T. Van Tran, *Nanoscale Adv.*, 2024, **6**, 1800–1821.
11 Y. Liu, K. K. Chui, X. Xia, H. Zhang, X. Zhuo and J. Wang, *Nano Res.*, 2024, **17**, 9166–9173.
12 D. Y. Fu, X. Liu, X. Zheng, M. Zhou, W. Wang, G. Su, T. Liu, L. Wang and Z. Xie, *Coord. Chem. Rev.*, 2022, **456**, 214393.
13 Y. Liu, H. Cheng, M. Cheng, Z. Liu, D. Huang, G. Zhang, B. Shao, Q. Liang, S. Luo, T. Wu and S. Xiao, *Chem. Eng. J.*, 2021, **417**, 127914.
14 X. Wang, H. Wang, J. Cheng, H. Li, X. Wu, D. Zhang, X. Shi, J. Zhang, N. Han and Y. Chen, *Chem. Eng. J.*, 2023, **466**, 143201.
15 J. S. Packialakshmi, J. Kang, A. Jayakumar, S. Park, Y. Chang and J. T. Kim, *Food Packag Shelf Life*, 2023, **40**, 101213.
16 C. Shen, Y. Xue, Y. Li, M. Wei, M. Wen, L. Zhang and L. Shang, *J. Mater. Sci. Technol.*, 2023, **162**, 145–156.
17 N. Tripathi and M. K. Goshisht, *ACS Appl. Bio. Mater.*, 2022, **5**, 1391–1463.
18 E. Zhang, X. Zhao, J. Hu, R. Wang, S. Fu and G. Qin, *Bioact Mater*, 2021, **6**, 2569–2612.
19 H. Dai, X. Yuan, L. Jiang, H. Wang, J. Zhang, J. Zhang and T. Xiong, *Coord. Chem. Rev.*, 2021, **441**, 213985.
20 N. T. Truc Phuong, V. Q. Dang, L. Van Hieu, T. N. Bach, B. X. Khuyen, H. K. Thi Ta, H. Ju, B. T. Phan and N. H. Thi Tran, *RSC Adv.*, 2022, **12**, 31352–31362.
21 L. G. Phuc, P. Q. T. Do, H. K. T. Ta, V. Q. Dang, S. W. Joo, D. H. Manh, T. N. Bach, T. T. T. Van and N. H. T. Tran, *Chemosensors*, DOI: **10.3390/chemosensors11010056**.
22 P. Q. T. Do, V. T. Huong, N. T. T. Phuong, T. H. Nguyen, H. K. T. Ta, H. Ju, T. B. Phan, V. D. Phung, K. T. L. Trinh and N. H. T. Tran, *RSC Adv.*, 2020, **10**, 30858–30869.
23 Y. Zhang, Y. Jia, M. Li and L. Hou, *Sci. Rep.*, 2018, **8**, 1–7.
24 D. Cheng, Y. Zhou, Q. Wang, X. Zhang, M. Li, Y. Lu, J. Xu, L. Zhang and J. Wang, *J. Phys. Chem. C*, 2022, **127**, 3542–3550.
25 G. Zuo, A. Wang, Y. Yang, H. Huang, F. Wang, H. Jiang, L. Zhang and Y. Zheng, *J. Porous Mater.*, 2019, **27**, 339–345.
26 X. Guo, S. He, Z. Meng, Y. Wang and Y. Peng, *RSC Adv.*, 2022, **12**, 17919–17931.
27 G. Nie, J. Xue, Y. Gao, Z. Wang, H. Wang, J. Wu, Y. Long and W. Han, *Microchem. J.*, 2025, **210**, 113007.
28 D. Zhang, M. He, C. Qin, Z. Wu, M. Cao, D. Ni, Z. Yu and P. Liang, *Spectrochim. Acta, Part A*, 2024, **308**, 123754.
29 A. Akhundzadeh Tezerjani, R. Halladj and S. Askari, *RSC Adv.*, 2021, **11**, 19914–19923.
30 M. M. Abdelkhalek, A. M. Mohamed, R. Z. Abdallah, G. E. Khedr, R. Siam and N. K. Allam, *Nanoscale Adv.*, 2024, **6**, 3355–3366.

31 S. Moniri, M. Reza Hantehzadeh, M. Ghoranneviss and M. Asadi Asadabad, *Eur. Phys. J. Plus*, 2017, **132**, 1–16.

32 X. Niu, S. Yan, R. Zhao, H. Li, X. Liu and K. Wang, *ACS Appl. Mater. Interfaces*, 2023, **15**, 22435–22444.

33 D. Chen, Y. Li, S. Xu, Z. Guo, Q. Yao and X. Chen, *Microchem. J.*, 2024, **200**, 110449.

34 T. K. H. Ta, M. T. Trinh, N. V. Long, T. T. M. Nguyen, T. L. T. Nguyen, T. L. Thuoc, B. T. Phan, D. Mott, S. Maenosono, H. Tran-Van and V. H. Le, *Colloids Surf., A*, 2016, **504**, 376–383.

35 P. Raju and S. Natarajan, *J. Inorg. Organomet. Polym. Mater.*, 2022, **32**, 2771–2780.

36 C. R. Quijia, R. C. Alves, G. Hanck-Silva, R. C. Galvão Frem, G. Arroyos and M. Chorilli, *Crit. Rev. Microbiol.*, 2022, **48**, 161–196.

37 H. Salari Joo, S. A. Johari, M. Behzadi Tayemeh, R. D. Handy, H. Abaei, N. Clark, J. Seyedi and M. A. Jones, *Environ. Pollut.*, 2024, **342**, 123141.

38 H. Salari Joo, M. Behzadi Tayemeh, H. Abaei and S. A. Johari, *Colloids Surf., A*, 2023, **668**, 131411.

39 G. Su, Y. Liu, Y. Hou, R. Zhang, W. Wang, J. Zhang and L. Dang, *ACS Appl. Mater. Interfaces*, 2024, **16**, 28080–28092.

40 A. Subhadarshini, S. K. Samal, A. Pattnaik and B. Nanda, *RSC Adv.*, 2023, **13**, 31756–31771.

41 X. Ren, L. Chang, Y. Hu, X. Zhao, S. Xu, Z. Liang, X. Mei and Z. Chen, *Mater. Des.*, 2023, **229**, 111890.

42 S. Londhe, S. Haque and C. R. Patra, *Gold and Silver Nanoparticles: Synthesis and Applications*, 2023, pp. 247–290.

43 Y. Bide and Z. Torabian, *Surf. Interfaces*, 2024, **50**, 104435.

44 N. Thomas, D. D. Dionysiou and S. C. Pillai, *J. Hazard. Mater.*, 2021, **404**, 124082.

45 H. Safajou, Z. M. Mizwari, A. Rostaminia, H. Khojasteh, P. Aspoukeh and M. P. Mazhari, *J. Fluoresc.*, 2024, 1–20.

46 F. E. Alzhrani, M. Gull, A. N. Khan, M. Aslam, W. A. Bawazir, N. M. Bataweel, A. M. Al-hejin, A. Hameed and M. T. Soomro, *Next Mater.*, 2025, **8**, 100542.